ACS APPLIED MATERIALS & INTERFACES

Research Article

www.acsami.org

Photoactive Porous Silicon Nanopowder

Benjamin H. Meekins,[†,‡,∥] Ya-Cheng Lin,[‡,∥] Joseph S. Manser,[†,‡,∥] Khachatur Manukyan,[‡] Alexander S. Mukasyan,[‡] Prashant V. Kamat,[†,‡,§] and Paul J. McGinn*[,‡]

[†]Radiation Research Laboratory, [‡]Department of Chemical and Biomolecular Engineering, and [§]Department of Chemistry and Biochemistry, University of Notre Dame, Notre Dame, Indiana 46556, United States

ABSTRACT: Bulk processing of porous silicon nanoparticles (nSi) of 50−300 nm size and surface area of 25−230 m^2/g has been developed using a combustion synthesis method. nSi exhibits consistent photoresponse to AM 1.5 simulated solar excitation. In confirmation of photoactivity, the films of nSi exhibit prompt bleaching following femtosecond laser pulse excitation resulting from the photoinduced charge separation. Photocurrent generation observed upon AM 1.5 excitation of these films in a photoelectrochemical cell shows strong dependence on the thickness of the intrinsic silica shell that encompasses the nanoparticles and hinders interparticle electron transfer.

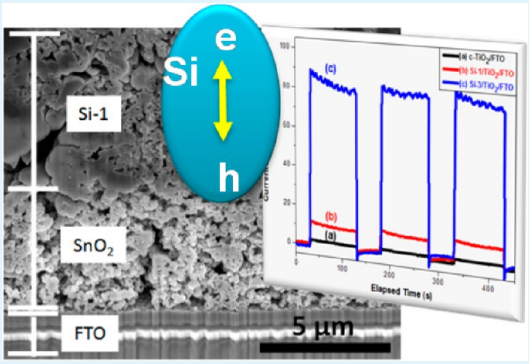

KEYWORDS: *solar energy, photoelectrochemistry, porous silicon, combustion synthesis, thermite reaction, nanopowder*

INTRODUCTION

Porous silicon has been the focus of research interest since the 1970s when the Uhlirs group attempted to develop an electrochemical method to fabricate silicon wafers for applications in microelectronic devices at Bell Laboratories. In the 1970s and 1980s, researchers found that the high surface area porous silicon was an attractive candidate for vapor sensors and spectroscopic applications.[1−3] In the 1980s and 1990s, more unique nanostructural characteristics of porous silicon (high surface area, increased reactivity) were observed, with many efforts dedicated to understanding the fundamentals of porous nanosilicon (nSi) and its use in electronics and biomedical sensors.[4] In addition, nSi has potential applications in thin film solar cells[5−7] and as an alternative for energetic materials.[8,9]

The large-scale mass production of nSi remains challenging. On the laboratory scale, different grades of nSi can be generated by stain etching[10,11] of either silicon wafers or metallurgical grade silicon powder in aqueous or nonaqueous electrolytes containing nitric acid (HNO_3) and hydrofluoric acid (HF). These techniques provide control over nSi pore-size distributions (mesoporous, macroporous) and the depth of etching, but fail to produce large quantities. This etching technique has been used to generate both random[6,12,13] and organized[14,15] silicon nanostructures.

On the industrial scale, silicon is typically produced via the reduction of silicon dioxide by carbon in high temperature furnaces.[16] This method is energy intensive and requires a processing time on the order of days. Two other similar methods of silicon production, aluminothermy and magnesium reduction, are also well-known.[17−19] However, all above conventional approaches do not allow bulk synthesis of silicon nanopowders.

Combustion synthesis (CS), also known as self-propagating high-temperature synthesis (SHS), is an attractive technique for production of different materials. In a conventional SHS scheme, a heterogeneous exothermic mixture of solid powders is pressed into a pellet and ignited at one end, generating a high-temperature combustion wavefront that propagates through the reactive media, converting the precursors to the desired product. The unique characteristics of CS include the following: (i) short (seconds) synthesis duration; (ii) great energy efficiency, since the internal system chemical energy is primarily used for materials production; (iii) requires only simple technological equipment; (iv) produces high purity products with unique properties since the extremely high temperatures in the combustion wave (up to 4000 K) burn off most of the impurities.

The combustion synthesis approach has also been used for nanomaterial production, including nSi.[20−22] However, there are some shortcomings related to CS that must be addressed. For example, in the selected thermite type (SiO_2/Mg) reaction, thermodynamic calculation predicts that the adiabatic combustion temperature is ∼2200 K, which is higher than the melting point of silicon (1687 K). This implies that as-formed silicon melts and agglomerates. To moderate the temperature, a modified CS route known as salt-assisted combustion synthesis (SACS)[23,24] is used. By combining the reactive mixture with

Received: July 13, 2012
Accepted: March 19, 2013
Published: March 19, 2013

 © 2013 American Chemical Society

alkali metal halides, the combustion temperature is significantly reduced, and the as-synthesized nanostructures are maintained.

The photoelectrochemical (PEC) properties of nanostructured silicon vary depending on the method of preparation.[25,26] Smestad and co-workers[27] measured an open circuit potential (V_{OC}) of 0.36 V and a short-circuit current (J_{SC}) of approximately 2 μA from a silicon wafer etched in HF. Greater photoactivity has been achieved with the use of silicon nanowire arrays. Liu and co-workers observed a J_{SC} of 27 mA/cm^2 in silicon nanowires formed by etching a silicon wafer in $AgNO_3$ and HF,[28] and Kelzenberg et al. achieved 23 mA/cm^2 in single p-n radial junction nanowires.[29] Syu et al.[30] created a solid-state silicon nanowire/PEDOT:PSS device with a maximum external quantum efficiency of 63%. Boettcher et al. used a silicon nanowire array with a discontinuous Pt layer to evolve hydrogen from water in a three-electrode system.[15]

We now report the bulk synthesis of porous silicon nanopowder (nSi) using a SACS method to explore the photoactivity of nSi. The results of the transient absorption spectroscopy and PEC measurements are presented and shortcomings of nSi along with possible solutions to address these limitations are discussed.

EXPERIMENTAL SECTION

Synthesis. The desired amount of Mg (99.8% purity, mean particle size $d \leq 44$ μm, Alfa Aesar, U.S.A.), SiO_2 (99.5%, $d \leq 44$ μm, Cerac, U.S.A.), and NaCl (Alfa Aesar, U.S.A.) powders were thoroughly mixed in an ethanol bath (ethanol:mixture 2:1 wt %) with zirconium oxide (ZrO_2) milling balls on a ball mill for 6 h, followed by drying in a temperature controlled oven at 353 K for 12 h. All powders utilized in this work were used as-received.

This SiO_2/Mg/αNaCl exothermic mixture was placed in a graphite crucible (6.5 cm O.D. × 5 cm I.D. × 5 cm deep) and inserted into a cylindrical steel reactor (26 cm O.D. × 23 cm I.D. × 60 cm length). The reactor was sealed, evacuated to $P_i = 10^{-5}$ MPa and then purged with argon gas (99.998% purity, Praxair Distribution Inc., U.S.A.) up to the desired pressure (P_f = 0.1−3 MPa). The combustion process was initiated by passing a DC pulse (I = 10 A, U = 20 V) through a tungsten wire located close to the powder surface in the graphite sleeve. The pulse was turned off immediately after reaction initiation. A combustion wave propagated in a self-sustained manner along the sample volume, converting the initial mixture into the final product. The overall SACS reaction can be expressed as follows:

$$SiO_2 + 2Mg + \alpha NaCl \rightarrow Si + 2MgO + \alpha NaCl, \quad 1 \leq \alpha \leq 2 \tag{1}$$

It is worth noting that up to 2.5 kg of nSi powder can be produced in one batch under these synthesis conditions. The as-synthesized product is then collected for further hydrometallurgical treatments and characterization.

Post-Treatment. The as-synthesized product was leached in an acid solution at room temperature to remove undesired phases like MgO and NaCl. In some cases, to obtain nSi with a higher purity, an additional leaching process using a combination of multiple acids at an elevated temperature was carried out. More specifically, the acid leaching of as-synthesized products was performed by a two-step procedure to remove metal impurities and to reduce oxygen (silica) content in the silicon. The first step included treatment in a dilute hydrochloric acid solution. After 6 h the as-leached materials were then vacuum-filtered and collected. For select powders, a second purification was carried out involving treatment of silicon powder with a multi-acid solution (40% water, 30% ethanol, 20% hydrofluoric acid, 5% nitric acid, and 5% acetic acid by volume) at 323 K for 3 h. An excess of deionized water was used to neutralize the acidic Si solution until neutral pH was reached. The final Si product was dried overnight at room temperature under vacuum.

Characterization. The phase compositions of nSi before and after synthesis and post-treatment were determined by X-ray diffraction (XRD, Scintag X1 Advanced Diffraction System, Scintag Inc., U.S.A.) operated at 40 kV and 30 mA. XRD Step-scan data (step size 0.02° and counting time 0.5 s) of nSi was recorded for the angular range 20−80°. The purity of the as-synthesized nSi (i.e., oxygen concentration) was determined by both energy dispersive X-ray spectroscopy (EDS) (INCAx-sight Model 7636; Oxford Instruments, U.S.A.) and an inert gas fusion method at Leco, Inc. (St. Joseph, MI, U.S.A.). Brunauer−Emmett−Teller (BET) specific surface area (SSA) was measured on a Coulter SA3100 analyzer at 77 K, with nitrogen as the adsorbent gas. The nSi was held under vacuum at 298 K for 4 h before the SSA measurement. nSi microstructural morphologies were examined by a field emission scanning electron microscope (FESEM, Magellan 400, FEI, U.S.A.). Atomic level structure analysis was performed on an FEI-Titan 80-300 transmission electron microscope (TEM) at 300 kV in a high-resolution transmission electron microscopy (HRTEM) mode.

PEC measurements were performed in a two-electrode configuration on a PARstat 2263 potentiostat (Princeton Applied Research). Both open and sandwich cell experimental setups (see schemes in Figure 7C and Figure 8, respectively) were used to test nSi PEC performance. An SnO_2 paste synthesized by literature methods[31] was used to prepare films for transient absorption and open cell PEC measurements. In brief, a colloidal solution of 700 mg of polyethylene glycol per mL of SnO_2 (15% aqueous solution, Alfa Aesar) was heated while stirring until well-mixed. This paste was applied by a doctor-blade method onto a glass substrate (microscope glass for transient absorption, fluorine-doped tin oxide (FTO) for PEC measurements) and annealed at 773 K for 1 h. This produced a porous SnO_2 nanoparticulate film that was approximately 4 μm thick. Porous silicon nanoparticle films used in the open cell setup and for transient absorption spectroscopy were generated using electrophoretic deposition. A 5 mg/mL solution of nSi in acetonitrile was used for deposition. Thirty V was applied for 30 s between two FTO electrodes held 4 mm apart. The films were then dried in a vacuum oven at 363 K for a minimum of 4 h to improve film integrity.

Electrodes employed in sandwich cells were first treated with a 40 mM aqueous $TiCl_4$ solution (Alfa Aesar, 99%) at 343 K for 30 min, followed by washing with deionized water and ethanol. The electrodes were then sintered at 773 K for 1 h to form a protective compact TiO_2 layer (c-TiO_2). nSi films were cast over the compact layer by doctor-blading a paste of nSi suspended in *tert*-butanol (Fisher Scientific) and deionized water. The paste was adapted from literature methods[32] and consisted of 0.5 mL of solution (2:1 *tert*-butanol:water) per 100 mg of nSi powder. The mixture was stirred for at least 24 h prior to deposition, yielding a relatively viscous solution. Films were subsequently dried under vacuum as noted above.

A 300 W Xe lamp (Oriel) with an AM 1.5 filter (Newport) was used as the illumination source. The working sample was placed at the point where incident power was measured to be 100 mW/cm^2 by a Scientech 365 power meter. Platinum mesh served as the counter electrode for open cell PEC measurements, while platinum deposited on FTO was used for sandwich cell measurements. Platinum-on-FTO counters were prepared by treating FTO electrodes with a 2 mg/mL solution of H_2PtCl_6 (Sigma Aldrich, 99.995%) in ethanol and annealing at 673 K for 20 min. Before all PEC measurements, electrolyte solutions were degassed for a minimum of 30 min to remove oxygen from the system. During open cell PEC experiments, nitrogen was allowed to flow over the sulfuric acid (H_2SO_4) electrolyte to prevent oxygen re-entry.

Dimethylferrocenium tetrafluoroborate (Me_2FcBF_4) was synthesized by dissolving 0.2 g of 1,1′-dimethylferrocene (Alfa Aesar, 97%) in 10 mL of acetone. An equimolar amount of silver tetrafluoroborate (Alfa Aesar, 99%) was added to the solution. Silver immediately precipitated out, and the final dark blue solution was filtered, dried, and resuspended in acetonitrile. Me_2FcBF_4 was stored in a light-sensitive bottle under inert atmosphere. The $Me_2Fc^{0/+}$ electrolyte consisted of 0.2 M dimethylferrocene, 0.2 M dimethylferrocenium, and 1 M $LiClO_4$ as the supporting electrolyte in acetonitrile.

Transient absorption measurements were conducted using a Clark-MXR 2010 (775 nm, fwhm = 130 fs, 1 kHz repetition) laser system coupled with detection software from Ultrafast Systems (Helios). The pump-probe beams were incident on the sample (room temperature) at an angle <10°. The incident power at the sample was measured as 60 mW/cm^2. The probe beam was collected with a CCD spectrograph (Ocean Optics, S2000-UV-vis) providing a 430−750 nm data window. All optical measurements on films were conducted in an evacuated 5-mm path length quartz cell.

RESULTS AND DISCUSSION

Combustion Synthesis. Synthesis of silicon nanopowder by a thermite-type combustion method without the addition of any alkali metal halides has been reported by Yermekova et al.[20] In this study, solid sodium chloride was added to the binary SiO_2/Mg exothermic thermite-type reaction to produce nSi. The NaCl, as a representative of alkali metal halides, is utilized to control synthesis temperature and to preserve the nanostructure of the as-synthesized particles by preventing their sintering in the postcombustion zone. More specifically, when the salt concentration increases, the combustion temperature decreases. The molten salt also forms a protective layer around the particles, hindering a sintering process. At higher temperatures (i.e., low salt concentration), the mobility of molten salt is high and the protective effect is not as strong, which leads to increases in particle size.

The dependence of the adiabatic combustion temperature (T_{ad}, K) in SiO_2+2Mg systems as a function of molar concentration of NaCl (α) was calculated by the thermodynamic software package "THERMO".[33] Thermodynamic estimations (Figure 1) revealed that without the addition of NaCl the adiabatic combustion temperature of the SiO_2+2Mg system approaches 2200 K, well above the melting points of Mg (922 K), Si (1683 K), and SiO_2 (1923 K). This temperature is also above the boiling point of Mg (1363 K) but below the melting point of MgO (3073 K).

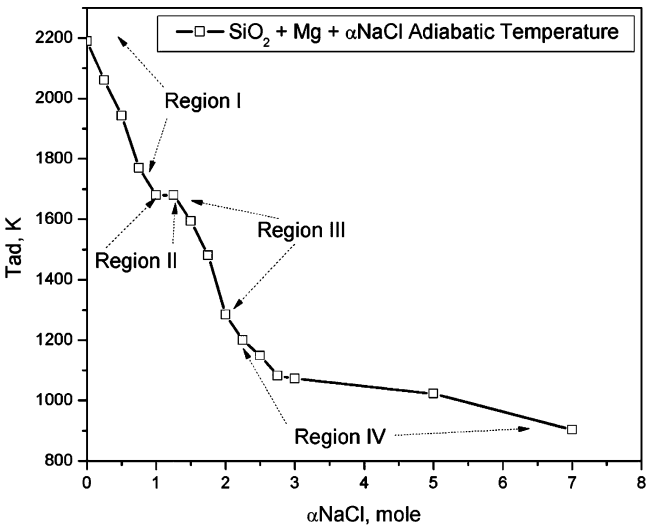

Figure 1. Thermodynamic characteristics of the SiO_2/Mg adiabatic combustion temperature (T_{ad}) as a function of NaCl addition (moles) at P_{Ar} = 2 MPa. All values were calculated using THERMO software.

It can also be seen that the T_{ad} shows a linear decrease in concentration in Region I ($0 \leq \alpha \leq 1$) and reaches a plateau in Region II ($1 \leq \alpha \leq 1.25$), where the adiabatic temperature corresponds to the melting point of silicon. This is followed by further temperature decrease in Region III ($1.25 \leq \alpha \leq 2$). At higher α (Region IV) the temperature is too low for a self-sustained combustion reaction. It is reasonable to choose dilution in Region III ($1.25 \leq \alpha \leq 2$), which corresponds to a moderate combustion temperature range 1284 K $\leq T_{ad} \leq$ 1680 K. This is below both the melting point of Si and the boiling point for sodium chloride (1686 K), but above the mp of NaCl (1074 K). Indeed, even a short-term exposure to a higher temperature (T > 1687 K) in the combustion wave may cause the coarsening of as-synthesized silicon nanostructures by coalescence of melted Si particles. In practice, all the measured combustion temperatures are slightly lower than the calculated values for the investigated system.[24,28] In short, this effect can be explained by heat losses from the reactants to the graphite crucible and to the gas phase surroundings during the experiments, which leads to lower combustion temperatures than those predicted thermodynamically.

Parameters other than the extent of NaCl dilution (α), such as the pressure of inert gas (argon) in the reactor and the cooling rate in the postcombustion zone, can also influence the properties of CS-materials.[15] However, in this work the key factor for producing nSi powders with different surface areas and oxygen concentrations was the leaching conditions, which were applied to the powders synthesized under identical optimized combustion parameters. Of the more than 50 different varieties of nSi produced, three specific sets of nanopowders abbreviated as Si-1, Si-2, and Si-3 are discussed in this work. These powders were prepared by chemical treatments of as-synthesized products in 1.45 M HCl (Si-1), 11.75 M HCl (Si-2), and multiacid (Si-3) solutions.

Microstructure. Typical XRD patterns of initial reactants (trace a), as-synthesized products (trace b), and as-leached nSi (trace c) are shown in Figure 2. The initial mixture contains three crystalline phases (SiO_2, Mg, and NaCl). The as-synthesized product also has three crystalline phases (Si, MgO, and NaCl). After a hydrometallurgical treatment (i.e., acid leaching), only the crystalline silicon phase was detected (Figure 2, trace c).

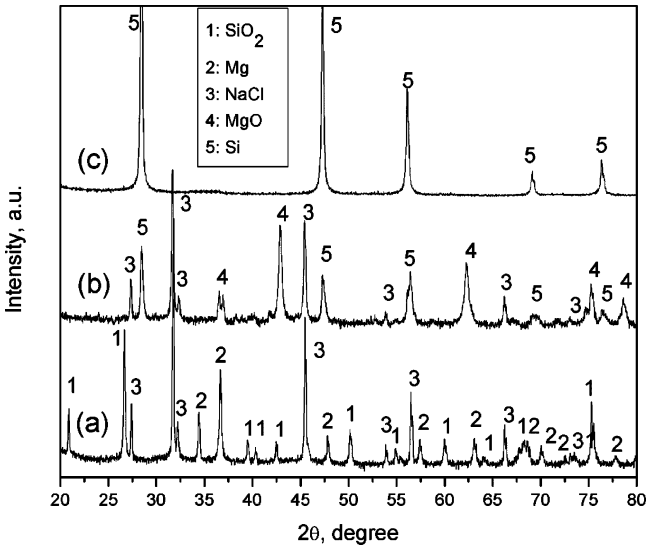

Figure 2. XRD patterns of the initial reactants (a), the as-synthesized products (b), and the nSi (Si-1) after leaching with HCl (c).

Typical SEM images of the initial reactants, as well as Si-1 and Si-2 powders are shown in Figure 3. The initial SiO_2 and

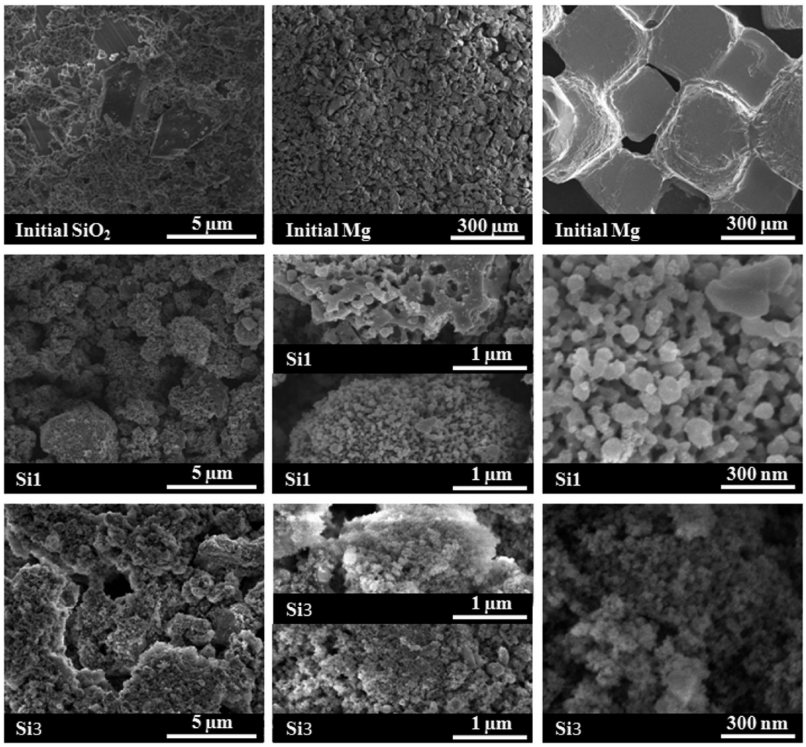

Figure 3. Typical SEM images of initial reactants (top row), the as-leached Si-1 (middle row), and Si-2 (bottom row).

Mg precursors have a wide micrometer-scale range of particle size distributions (1−5 μm for the SiO_2 and 5−50 μm for the Mg), while NaCl particles are uniform in size (∼300 μm) and shape. Note that Si-1 and Si-3 powders possess essentially identical microstructures, therefore only typical morphologies for Si-1 and Si-2 samples are compared. Both theses powders include porous silicon agglomerates in the 1−2 μm range. However, at a higher magnification, it can be seen that the Si-1 powder primarily consists of particles with an average size of 40 nm, while Si-2 contains smaller particulates with diameters below 20 nm. Such morphologies and size ranges of individual particles allow us to classify these powders as porous nanosilicon.

Table 1 summarizes leaching conditions, BET SSA, and oxygen concentration data for the three Si powders. It is shown that leaching in hydrochloric acid of higher concentration leads to nSi with higher SSA (Si-1: 45 and Si-2: 230 m^2/g); however, the amount of oxygen in the powder also increases (Si-1: 3 and Si-2: 14 wt %). It is important to note that an additional treatment in a multiacid solution results in significant reduction of oxygen (Si-3: 0.2 wt %) with only a slight decrease in powder SSA (compare Si-1 and Si-3).

Table 1. BET SSA and Oxygen Concentration for Silicon Powders Leached under Different Conditions

	leach-step 1		leach-step 2		
	HCl	concentration	multi-Acid	BET	chemical analysis
unit		M		m^2/g	oxygen (wt %)
Si-1	X	1.45		45	3
Si-2	X	11.75		230	14
Si-3	X	1.45	X	25	0.2

TEM bright field and HRTEM electron images and selected area diffraction patterns (SADP) for the powders are shown in Figure 4. Statistical analysis reveals that all powders are composed of two types of particles: (1) nanometric particulates less than 100 nm in size and (2) relatively large submicrometer particles with diameters in the range of 200−300 nm. Figures 4A1, 4B1, and 4C1 show HRTEM images of the small silicon nano particulate surface structures. Figures 4A2, 4B2 and 4C2 show large silicon agglomerate surface structures. The differences in nSi powders are the relative amount of these two morphologies, morphology crystallinity, and oxygen concentration.

Figure 4A illustrates a typical low-magnification TEM image of the Si-1 powder. It can be seen that submicrometer particles with average diameter of 200 nm are surrounded by smaller nano particulates with sizes less than 40 nm. Figure 4A1 shows a typical HRTEM image and SADP pattern of the Si-1 nano particulates. In addition, one should note that in Figure 4A1 most grains are crystalline, which is confirmed by the corresponding SADP. Some amorphous areas were also detected. Statistical EDS analysis of such areas shows that their average oxygen concentration is ∼23 wt %. The HRTEM image in Figure 4A2 shows a representative submicrometer particle in the Si-1 sample. The highly crystalline core is covered by a thin (<5 nm) amorphous phase. EDS analysis reveals negligible oxygen content in the particle bulk and >30 wt % in the amorphous layer.

Figure 4B represents a typical low-magnification TEM image for the Si-2 powder, which was leached in hydrochloric acid solution of higher concentration. While again both nano and submicrometer morphologies can be seen, the relative amount of the nano morphology is higher as compared to sample Si-1. It is more interesting that HRTEM images as well as SADPs show that nanoparticulates are essentially amorphous (Figure 4B1), and the amorphous layer on the surface of the

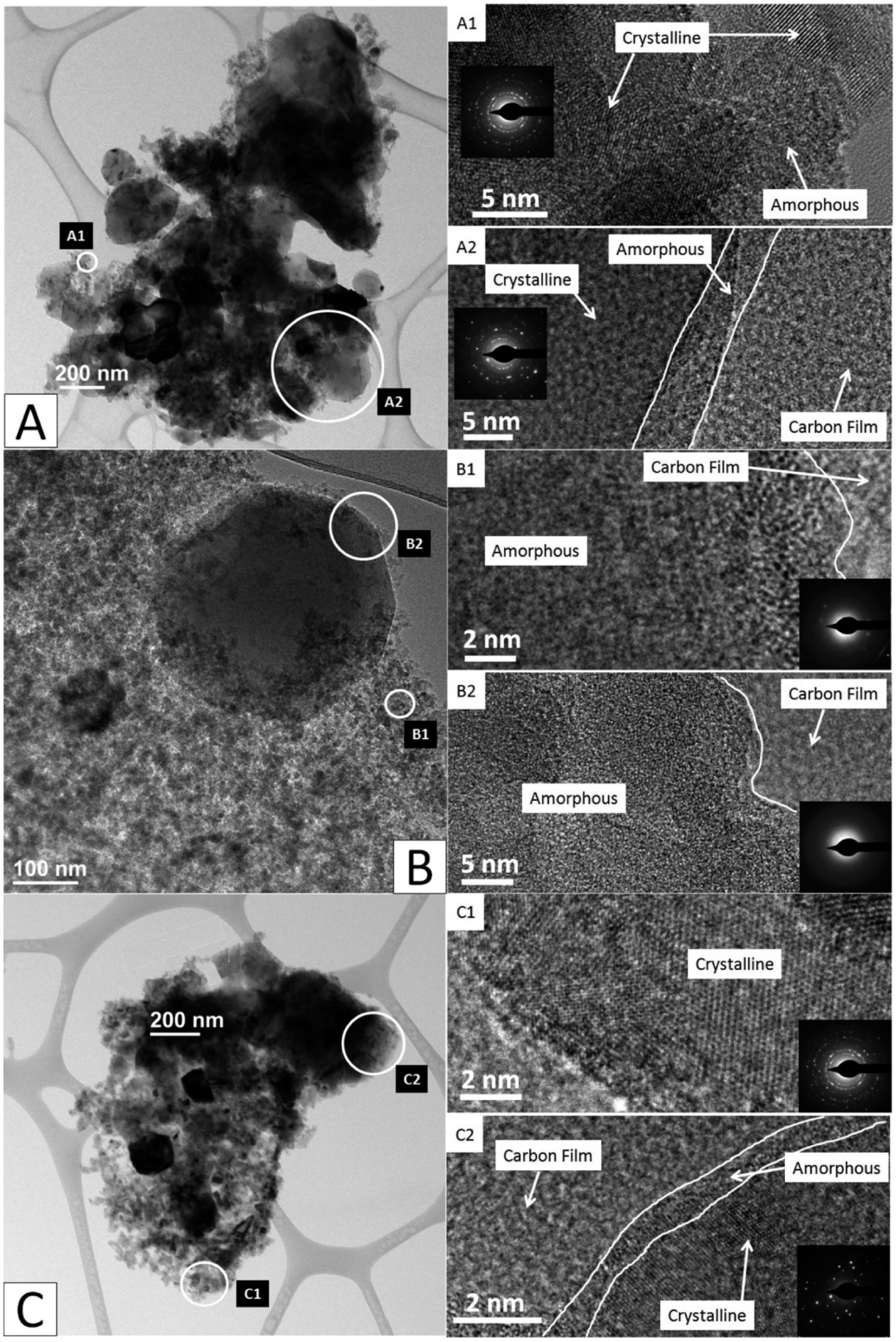

Figure 4. Typical TEM images of Si-1 (A), Si-2 (B), and Si-3 (C). Note that the circled areas indicate regions where SADPs were taken. A1, B1, and C1 show HRTEM images of small silicon nano particulate surface structures. A2, B2, and C2 show large silicon agglomerate surface structures.

submicrometer (350 nm) particle (Figure 4B2) is also relatively large at ∼30 nm. EDS analysis shows oxygen concentrations of <2 wt % and ∼30 wt % in the bulk of submicrometer particles and in the area of nano particulates, respectively. The obtained data reveal that the high surface area (∼230 m^2/g) of the Si-2 powder is due to large amounts of highly oxidized nano particulates. This feature leads to a high average oxygen concentration (14 wt %) in the powder.

As mentioned above, Si-1 and Si-3 powders are morphologically similar, and comparison of Figures 4A and 4C confirms this conclusion. However, HRTEM images also reveal some subtle differences. It can be seen that almost all nano particulates are crystalline in the Si-3 sample (Figure 4C1),

and the thickness of the amorphous oxygen-containing layer on the surface of the submicrometer particles (Figure 4C2) is thinner (~1 nm). Leaching in a multiacid solution results in dissolution of the amorphous phase which contains relatively large amounts of oxygen, leading to a more pure (0.2 wt %) powder, but with slightly lower SSA.

These three different silicon nanopowders that vary widely in SSA (25−230 m^2/g), oxygen concentration (0.2−14 wt %), and crystallinity were tested for their PEC properties.

Deposition of Si Nanopowders on Optically Transparent Electrodes (OTEs). nSi films were cast on conducting glass electrodes by electrophoretic deposition (EPD) and by doctor-blade method for open and sandwich cells, respectively. EPD utilizes an electric field to drive charged particles suspended in a suitable solvent to an oppositely charged electrode. This deposition method generates robust films. It can be seen in Figures 5A and 5B that the electrophoretically deposited silicon nanoparticles are generally aggregated on top of the porous SnO_2 network. The nanostructured SnO_2 layer increases the surface area of the electrode, providing a larger number of sites for collecting charges from the excited nSi film. nSi absorbs throughout the visible and near-infrared regions (Figure 5C). The observed absorption onset is seen at 1050 nm, corresponding to a bandgap of approximately 1.18 eV. This bandgap is close to the bulk bandgap of Si which one expects to be around 1.12 eV.

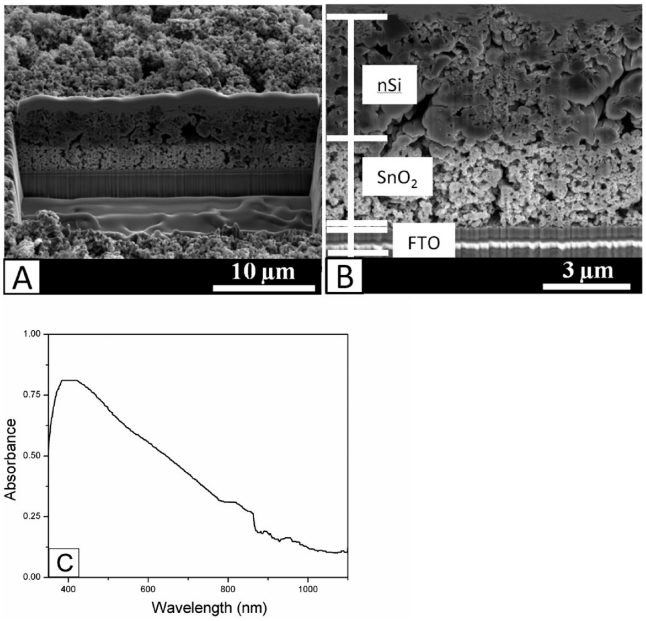

Figure 5. (A and B) Cross section of the as-deposited Si-1 film on an optically transparent FTO electrode. (A) Low magnification image of layering of Si-1, SnO_2, and FTO layers. (B) Magnified image showing more details of the cross-section. The thickness of the SnO_2 layer is approximately 3 μm while the thickness of the Si-1 layer is approximately 4.5 μm. Note that the large agglomerates result from the redeposition of vaporized material during focused ion beam etching used to generate the cross-section. (C) Diffuse reflectance (recorded in the absorbance mode) of the silicon film deposited on an FTO electrode.

Transient Absorption Spectroscopy. Femtosecond transient absorption spectroscopy is a convenient technique to probe the photoinduced charge separation in semiconductor nanostructures. Earlier studies have extensively employed this technique to investigate the excited state dynamics of metal chalcogenides and silicon nanowires.[14,31,34] Relatively fewer studies have been conducted to explore the charge separation in Si nanostructures.[14] Time-resolved transient absorption spectra recorded following 387 nm laser pulse excitation of the nanostructured Si-1 film are shown in Figure 6A. The bleaching seen across the entire visible region confirms the disappearance of the absorption as a result of photoexcitation of Si-1 films (SSA 45 m^2/g; oxygen content ~3−4 wt %). With increasing time the bleaching recovers as the electrons and holes undergo recombination. Thus, the transient bleaching can be used as a probe to monitor charge separation. The ultrafast recovery seen within 50 ps indicates fast charge recombination within the Si-1 film.

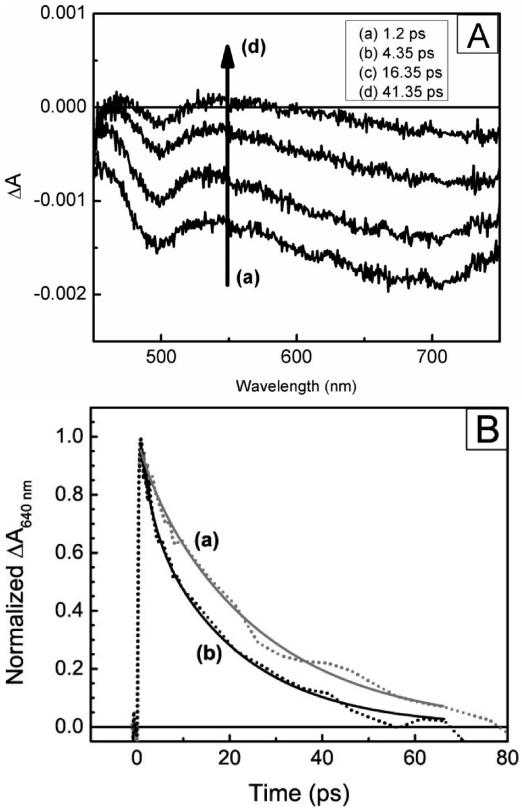

Figure 6. (A) Bleaching recovery of Si-1 deposited on an SnO_2 layer with spectra at (a) 1.2 ps, (b) 4.35 ps, (c) 16.35 ps, and (d) 41.35 ps after the excitation pulse. (B) Absorption-time profile showing the bleaching recovery (dotted lines) and biexponential fits (solid lines) of (a) Si-1 on SiO_2 and (b) Si-1 on SnO_2 recorded at 640 nm. For transient absorption measurements, films were kept under vacuum in a closed cell. Excitation power was 60 mW per cm^2. The spectrum and kinetic traces are the average of three separate experimental runs.

These transient absorption characteristics parallel the reports of Wheeler and co-workers[14] who synthesized silicon nanowires by etching a silicon wafer. They too reported a broad bleaching in the visible region (500 to 770 nm) and a multiexponential recovery. The lifetime of the bleaching recovery in Figure 6A was fit with a biexponential decay function composed of a short (τ_s) and long component (τ_l). The fitting parameters are summarized in Table 2. The short component corresponds to trapping of photogenerated charges (in the case of the porous silicon nanoparticles on SiO_2) or a convolution of charge trapping and electron transfer (in the case of porous silicon

Table 2. Biexponential Fitting Parameters with Their Uncertainty for the Transient Absorption Kinetic Traces[a]

	A_s	τ_s, ps	A_l	τ_l, ns
Si-1/SiO_2	0.92 ± 0.03	25.87 ± 1.13	0.08 ± 0.02	3.26 ± 1.98
Si-1/SnO_2	0.64 ± 0.14	21.86 ± 3.30	0.36 ± 0.13	5.52 ± 1.80

[a]See Figure 6B. The electron transfer rate was calculated using the short component of the fit (τ_s).

nanoparticles on SnO_2). Figure 6B shows kinetic traces of the bleach decay and the fits for silicon on SiO_2 and SnO_2. If we assume that electron transfer is the only additional pathway for bleaching recovery in the Si-1/SnO_2 system, we can calculate an electron transfer rate based on the biexponential fit of the kinetic traces using eq 2:[35]

$$k_T = \frac{1}{\tau_{s,SnO_2}} - \frac{1}{\tau_{s,SiO_2}} \quad (2)$$

where τ_{s,SnO_2} and τ_{s,SiO_2} are the short lifetime components for the Si-1/SnO_2 and Si-1/SiO_2 systems, respectively. By this calculation the electron transfer rate was 7.1×10^9 s^{-1}.

PEC Characterization. If indeed the excitation of nSi is responsible for charge separation as seen in the transient absorption spectroscopy measurements, we should be able to capture these charges for photocurrent generation. To probe the photoresponse we carried out PEC measurements using nSi films as photoactive electrodes. Earlier studies have employed single crystal Si and nanostructured silicon wire based electrodes for photocurrent generation[36] and/or water splitting reaction.[15] The electrolytes employed in these studies include acidic solutions and redox couples (e.g., ferrocene). Here we explore the PEC characteristics of nSi in both 0.1 M H_2SO_4 and a regenerative dimethylferrocene/dimethylferrocenium redox couple ($Me_2Fc^{0/+}$). It is important to note that the PEC cells utilized in this study operate on the principles of interfacial charge transfer kinetics which dictate the overall photocurrent generation. We tested the photoresponse of nSi electrodes (Si-1 and Si-3, see Table 1 for characteristics) in two separate experiments to assess their performance in the different electrolyte solutions.

Figure 7A shows the open circuit photovoltage of Si-1 produced under AM 1.5 conditions in an open cell configuration with 0.1 M H_2SO_4 serving as the electrolyte. The negative photovoltage seen under illumination indicates that the porous silicon is n-type. This n-type behavior was also confirmed from the photocurrent measurements (Figure 7B). Whereas nSi produced reasonable photovoltage response, the observed photocurrents were too low to make a significant impact in the PEC investigation. Given the observed n-type nature of nSi, one should expect improved performance in the presence of an electron donor system in the electrolyte.

The next set of experiments were carried out using the $Me_2Fc^{0/+}$ electrolyte. The $Me_2Fc^{0/+}$ electrolyte has been used extensively in high-efficiency liquid junction silicon photovoltaic cells and is known to form a favorable contact with silicon photoanodes.[37,38] To optimize the performance of these cells, we employed a sandwich cell configuration. Studies have shown that ferrocenium rapidly decomposes to iron(III) oxide and an organic polymer in the presence of atmospheric oxygen.[39−41] Therefore, oxygen contamination must be strictly avoided during PEC measurements. This fact, along with the strong visible absorption of $Me_2Fc^{0/+}$, motivated the change in configuration to a sandwich design. It is important to note that there were issues with the $Me_2Fc^{0/+}$ electrolyte scavenging

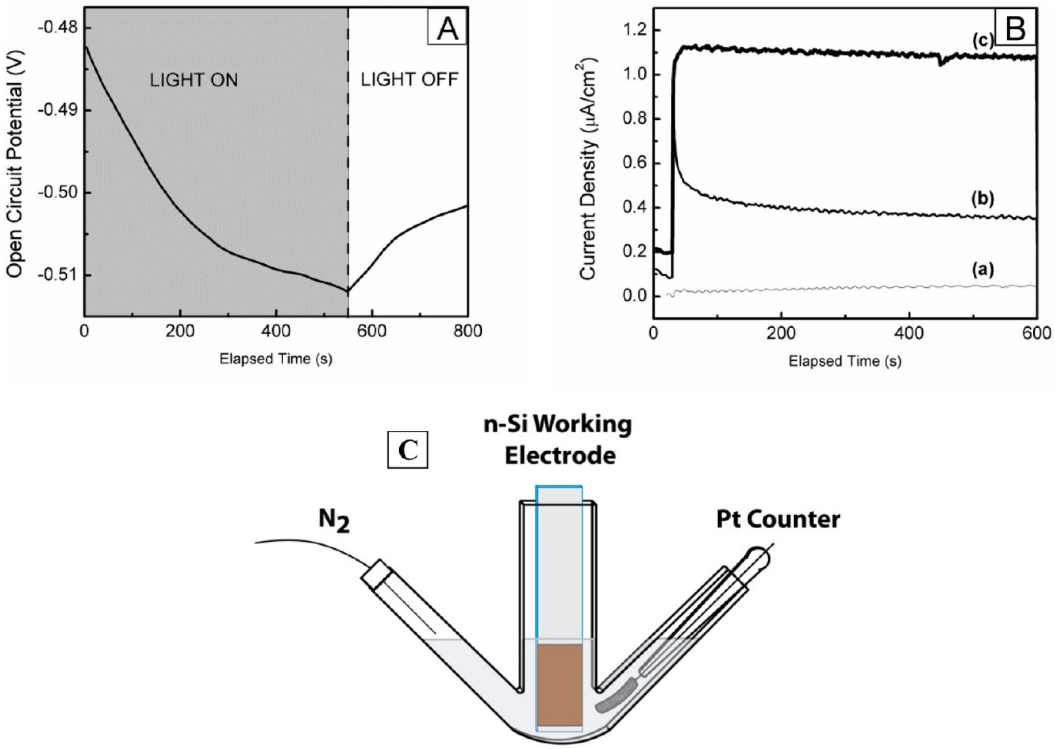

Figure 7. (A) Response of open circuit potential to on−off cycles of illumination. (B) Short circuit current response of (a) Si-1/FTO, (b) SnO_2/FTO, and (c) Si-1/SnO_2/FTO under AM 1.5 irradiation. (C) Schematic of the open cell two-electrode system with platinum mesh as the counter electrode and 0.1 M H_2SO_4 as the electrolyte.

electrons from the working electrode, which necessitated the deposition of a protective compact TiO_2 (c-TiO_2) layer. This 20−30 nm layer prevents short circuiting in the cell by blocking direct contact between the electrolyte and electrode surface, and is often used in PEC cells of this nature.[42]

Figure 8 shows the photocurrent response of both Si-1 and Si-3 in $Me_2Fc^{0/+}$ in sandwich cell configurations. Si-1 showed stable current at 10 $\mu A/cm^2$. The photocurrent response for Si-3 was approximately 80 $\mu A/cm^2$. This is nearly an order of magnitude higher than photocurrent generated by Si-1 in the same setup, and 2 orders of magnitude improvement over the original design with H_2SO_4 serving as the electrolyte. Because Si-3 has a thinner oxide shell (oxygen content ∼0.2 wt %) than Si-1 (oxygen content ∼3−4 wt %), electron transport between particles is vastly improved, resulting in higher photocurrent generation. This argument is in agreement with Monte Carlo simulations which predict an inverse exponential relation between the oxide thickness separating silicon particles and electron mobility, with mobility dropping approximately 2 orders of magnitude for every 0.5 nm increase in the oxide shell.[43] The lower surface area of Si-3 also contributed to the enhancement because of reduced hopping between particles.[44,45]

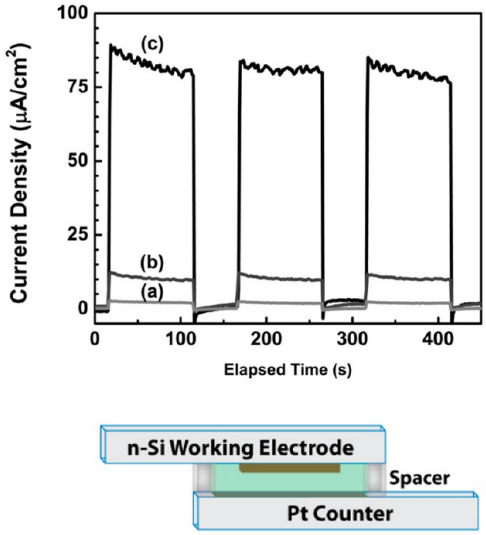

Figure 8. Top: photocurrent response under AM 1.5 illumination of (a) c-TiO_2/FTO, (b) Si-1/c-TiO_2/FTO, and (c) Si-3/c-TiO_2/FTO in the $Me_2Fc^{0/+}$ electrolyte with a platinum-on-FTO counter electrode. All measurements were carried out in sandwich configurations. Bottom: scheme showing a cross section of the sandwich cell assembly with an active area of approximately 0.35 cm^2.

We attribute the overall low level of PEC performance to two primary issues: (1) the insulating silica shell that encompasses individual particles or particle agglomerations acting as a barrier to interparticle electron hopping and (2) the short-lived charge separation in these Si nanocrystallites which inhibits efficient capture and transport of photogenerated electrons to the collecting electrode surface. Proper surface modifications, similar to those performed by Stutzmann et al.,[46] as well as particle doping are crucial to overcome these barriers and achieve significant enhancement in the photoactivity of these films.

CONCLUSION

Combustion synthesis of silicon nanopowder produces a highly crystalline photoactive material. Electron injection from Si-1 to SnO_2 was observed to occur on a picosecond time scale at a rate of 7.1×10^9 s^{-1}. PEC experiments revealed an n-type semiconductor response and measurable photoactivity under AM 1.5 illumination. The major barriers that must be overcome to improve PEC performance are the inherent silica shell that surrounds each Si nanoparticle and the fast charge recombination within the intrinsic particles as well as at particle interfaces. Modified syntheses are being developed to dope the silicon with both p- and n-type dopants, which should improve collection of photogenerated charge carriers within the film.

AUTHOR INFORMATION

Corresponding Author

*Tel: +1-574-631-6151. Fax: +1-574-631-8366. E-mail: pmcginn@nd.edu.

Author Contributions

‖These authors contributed equally.

Notes

The authors declare no competing financial interest.

ACKNOWLEDGMENTS

This work was supported by a grant from the Notre Dame Sustainable Energy Initiative. This work was also partially supported by the Notre Dame Center for Environmental Science and Technology (CEST) and the Notre Dame Integrated Imaging Facility (NDIIF). This is NDRL-4962 from the Notre Dame Radiation Laboratory which is supported by the Division of Chemical Sciences, Geosciences, and Biosciences, Office of Basic Energy Sciences of the U.S. Department of Energy.

REFERENCES

(1) Gupta, P.; Colvin, V.; George, S. *Phys. Rev. B: Condens. Matter Mater. Phys.* **1988**, *37*, 8234−8243.
(2) Dillon, A. C. *J. Electrochem. Soc.* **1992**, *139*, 537.
(3) Erson, R. C.; Muller, R. S.; Tobias, C. W. *Sens. Actuators, A* **1990**, *23*, 835−839.
(4) Sailor, M. J. In *Properties of Porous Silicon*; Canham, L., Ed.; Short Run Press Ltd.: London, U.K., 1997; pp 364−370.
(5) Oh, J.; Deutsch, T. G.; Yuan, H. C.; Branz, H. M. *Energy Environ. Sci.* **2011**, *4*, 1690.
(6) Mathews, N.; Sebastian, P.; Mathew, X.; Agarwal, V. *Int. J. Hydrogen Energy* **2003**, *28*, 629−632.
(7) Bahruji, H.; Bowker, M.; Davies, P. R. *Int. J. Hydrogen Energy* **2009**, *34*, 8504−8510.
(8) McCord, P.; Yau, S. L.; Bard, A. J. *Science* **1992**, *257*, 68−69.
(9) Plessis, M. D. *Sens. Actuators, A* **2007**, *135*, 666−674.
(10) Li, X.; Bohn, P. W. *Appl. Phys. Lett.* **2000**, *77*, 2572.
(11) Vázsonyi, É.; Szilágyi, E.; Petrik, P.; Horváth, Z. .; Lohner, T.; Fried, M.; Jalsovszky, G. *Thin Solid Films* **2001**, *388*, 295−302.
(12) Maiolo, J. R.; Atwater, H. A.; Lewis, N. S. *J. Phys. Chem. C* **2008**, *112*, 6194−6201.
(13) Lévy-Clément, C.; Lagoubi, A.; Ballutaud, D.; Ozanam, F.; Chazalviel, J. N.; Neumann-Spallart, M. *Appl. Surf. Sci.* **1993**, *65−66*, 408−414.
(14) Wheeler, D. A.; Huang, J. A.; Newhouse, R. J.; Zhang, W. F.; Lee, S. T.; Zhang, J. Z. *J. Phys. Chem. Lett.* **2012**, *3*, 766−771.
(15) Boettcher, S. W.; Warren, E. L.; Putnam, M. C.; Santori, E. A.; Turner-Evans, D.; Kelzenberg, M. D.; Walter, M. G.; McKone, J. R.; Brunschwig, B. S.; Atwater, H. A.; Lewis, N. S. *J. Am. Chem. Soc.* **2011**, *133*, 1216−1219.

(16) Koch, E. C.; Clément, D. *Propellants, Explos., Pyrotech.* **2007**, *32*, 205−212.
(17) Bao, Z.; Weatherspoon, M. R.; Shian, S.; Cai, Y.; Graham, P. D.; Allan, S. M.; Ahmad, G.; Dickerson, M. B.; Church, B. C.; Kang, Z.; Abernathy, H. W.; Summers, C. J.; Liu, M.; Sandhage, K. H. *Nature* **2007**, *446*, 172−175.
(18) Wynnyckyj, J. R.; Rao, D. B. *High Temp. Sci.* **1976**, *8*, 203−217.
(19) Banerjee, H. D.; Sen, S.; Acharya, H. N. *Mater. Sci. Eng.* **1982**, *52*, 173−179.
(20) Yermekova, Z.; Mansurov, Z.; Mukasyan, A. S. *Int. J. Self-Propag. High-Temp. Synth.* **2010**, *19*, 94−101.
(21) Hwang, S.; Mukasyan, A. S.; Varma, A. *Combust. Flame* **1998**, *115*, 354−363.
(22) Aruna, S. T.; Mukasyan, A. S. *Curr. Opin. Solid State Mater. Sci.* **2008**, *12*, 44−50.
(23) Nersisyan, H. H.; Lee, J. H.; Won, C. W. *J. Mater. Res.* **2011**, *17*, 2859−2864.
(24) Won, C. W.; Nersisyan, H. H.; Won, H. I.; Lee, J. H. *Curr. Opin. Solid State Mater. Sci.* **2010**, *14*, 53−68.
(25) Švrček, V.; Cook, S.; Kazaoui, S.; Kondo, M. *J. Phys. Chem. Lett.* **2011**, *2*, 1646−1650.
(26) Tao, M. *Electrochem. Soc. Interface* **2008**, *17*, 30−35.
(27) Smestad, G.; Kunst, M.; Vial, C. *Sol. Energy Mater. Sol. Cells* **1992**, *26*, 277−283.
(28) Liu, C. W.; Cheng, C. L.; Dai, B. T.; Yang, C. H.; Wang, J. Y. *Int. J. Photoenergy* **2012**, *2012*, 1−8.
(29) Kelzenberg, M. D.; Turner-Evans, D. B.; Putnam, M. C.; Boettcher, S. W.; Briggs, R. M.; Baek, J. Y.; Lewis, N. S.; Atwater, H. A. *Energy Environ. Sci.* **2011**, *4*, 866.
(30) Syu, H. J.; Shiu, S. C.; Lin, C. F. *Sol. Energy Mater. Sol. Cells* **2012**, *98*, 267−272.
(31) Tvrdy, K.; Frantsuzov, P. A.; Kamat, P. V. *Proc. Natl. Acad. Sci. U. S. A.* **2011**, *108*, 29−34.
(32) Genovese, M. P.; Lightcap, I. V.; Kamat, P. V. *ACS Nano* **2012**, *6*, 865−872.
(33) Shiryaev, A. A. *Int. J. Self-Propag. High-Temp. Synth.* **1995**, 351−362.
(34) Chuang, C. H.; Lo, S. S.; Scholes, G. D.; Burda, C. *J. Phys. Chem. Lett.* **2010**, *1*, 2530−2535.
(35) Kongkanand, A.; Tvrdy, K.; Takechi, K.; Kuno, M.; Kamat, P. V. *J. Am. Chem. Soc.* **2008**, *130*, 4007−4015.
(36) Maiolo, J. R.; Kayes, B. M.; Filler, M. A.; Putnam, M. C.; Kelzenberg, M. D.; Atwater, H. A.; Lewis, N. S. *J. Am. Chem. Soc.* **2007**, *129*, 12346−12347.
(37) Gibbons, J. F.; Cogan, G. W.; Gronet, C. M.; Lewis, N. S. *Appl. Phys. Lett.* **1984**, *45*, 1095.
(38) Laibinis, P. E.; Stanton, C. E.; Lewis, N. S. *J. Phys. Chem.* **1994**, *98*, 8765−8774.
(39) Zotti, G.; Schiavon, G.; Zecchin, S.; Favretto, D. *J. Electroanal. Chem.* **1998**, *456*, 217−221.
(40) Noviandri, I.; Brown, K. N.; Fleming, D. S.; Gulyas, P. T.; Lay, P. A.; Masters, A. F.; Phillips, L. *J. Phys. Chem. B* **1999**, *103*, 6713−6722.
(41) Bashkin, J. K.; Kinlen, P. J. *Inorg. Chem.* **1990**, *29*, 4507−4509.
(42) Rühle, S.; Yahav, S.; Greenwald, S.; Zaban, A. *J. Phys. Chem. C* **2012**, *116*, 17473−17478.
(43) Lepage, H.; Kaminski-Cachopo, A.; Poncet, A.; Le Carval, G. *J. Phys. Chem. C* **2012**, *116*, 10873−10880.
(44) Kang, M. S.; Sahu, A.; Norris, D. J.; Frisbie, C. D. *Nano Lett.* **2010**, *10*, 3727−3732.
(45) Liu, Y.; Gibbs, M.; Puthussery, J.; Gaik, S.; Ihly, R.; Hillhouse, H. W.; Law, M. *Nano Lett.* **2010**, *10*, 1960−1969.
(46) Niesar, S.; Pereira, R. N.; Stegner, A. R.; Erhard, N.; Hoeb, M.; Baumer, A.; Wiggers, H.; Brandt, M. S.; Stutzmann, M. *Adv. Funct. Mater.* **2012**, *22*, 1190−1198.